

# Comparisons of laboratory scale measurements of three-dimensional acoustic propagation with solutions by a parabolic equation model

Frédéric Sturm<sup>a)</sup> and Alexios Korakas

Laboratoire de Mécanique des Fluides et d'Acoustique—Unité Mixte de Recherche, Centre National de la Recherche Scientifique 5509 ECL-UCBL1-INSA de Lyon, Ecole Centrale de Lyon, F-69134 Ecully Cedex, France

(Received 25 June 2012; revised 16 October 2012; accepted 20 November 2012)

In this paper, laboratory scale measurements of long range across-slope acoustic propagation in a three-dimensional (3-D) wedge-like environment are compared to numerical solutions. In a previous work, it was shown that the experimental data contain strong 3-D effects like mode shadow zones and multiple mode arrivals, in qualitative agreement with theoretical and numerical predictions. In the present work, the experimental data are compared with numerical solutions obtained using a fully 3-D parabolic equation based model. A subspace inversion approach is used for the refinement of some of the parameters describing the model experiment. The inversion procedure is implemented in a Bayesian framework based on the exhaustive search over the parameter space. The comparisons are performed both in the time and in the frequency domain using the maximum *a posteriori* estimates of the refined parameters as input in the 3-D model. A very good quantitative agreement is achieved between the numerical predictions provided by the 3-D parabolic equation model and the experimental data. © 2013 Acoustical Society of America.  
[http://dx.doi.org/10.1121/1.4770252]

PACS number(s): 43.30.Zk, 43.30.Dr, 43.30.Bp, 43.30.Gv [TD]

Pages: 108–118

## I. INTRODUCTION

The study of 3-D acoustic propagation in realistic oceanic environments has received a lot of attention during the last three decades (see, for instance, Ref. 1, and references therein). More recently, renewed interest stimulated by experimental evidence of 3-D propagation<sup>2–6</sup> has given rise to an increasing number of publications reporting developments in theoretical and numerical 3-D modeling.<sup>7–13</sup> Of particular importance is the establishment of test cases for 3-D model validation and performance comparison. Significant efforts have been put into establishing benchmark solutions to canonical test cases,<sup>14</sup> among which notable is the 3-D ASA wedge problem simulating a continental shelf environment. However, unlike in 2-D propagation problems,<sup>15,16</sup> experimental measurements of 3-D propagation having the potential of being established as real-data benchmarks are rare in the literature.

In this context, two laboratory-scale experimental campaigns were led in 2006 and 2007 in the large indoor tank of the LMA-CNRS laboratory in Marseille, aimed at collecting 3-D acoustic propagation data over a tilted bottom in a well-controlled environment. The first campaign mainly consisted of preliminary tests, whereas the second was intended to collect high quality data. Operational frequencies and water depths were chosen to produce a reduced number of modes in order to facilitate the analysis of modal propagation in the wedge-like waveguide. In both campaigns, the experimental data exhibited prominent 3-D propagation effects like multi-

ple mode arrivals, mode shadow zones, intra-mode interference and focusing, all consistent with well-known 3-D effects described in the literature.<sup>1,17,18</sup> In addition, the data were in good qualitative agreement with both time- and frequency-domain simulations by a 3-D parabolic equation (PE)-based code<sup>19</sup> using the measured parameter values from the tank. Yet, quantitative comparisons turned out to be hindered by the uncertainties associated with some parameters, being large with respect to their potential impact on the acoustic field. Besides, improving the comparisons by blind testing of different sets of parameter values within their margins of uncertainty is a highly time-consuming task when comparing to 3-D model solutions.

In this paper, numerical results by a 3-D PE model are reported and compared to the 3-D propagation data collected during the second campaign. The parameter values used in the 3-D PE marching algorithm yielding the best match with the data are obtained using a subspace inversion approach based on the 3-D PE model. The present paper is organized as follows. The experimental set-up is recalled in Sec. II. The inversion procedure, implemented in a Bayesian framework, is detailed in Sec. III. Comparisons between experimental and numerical results are presented in Sec. IV both in the time and in the frequency domain. The paper closes with some concluding remarks. Preliminary results of the present work were presented during the 4th International Conference & Exhibition on Underwater Acoustic Measurements held in Kos, Greece in 2011.

## II. LABORATORY SCALE MEASUREMENTS

The scaled experiments presented here and considered in the remainder of this paper were conducted in July 2007

<sup>a)</sup>Author to whom correspondence should be addressed. Electronic mail: frederic.sturm@ec-lyon.fr

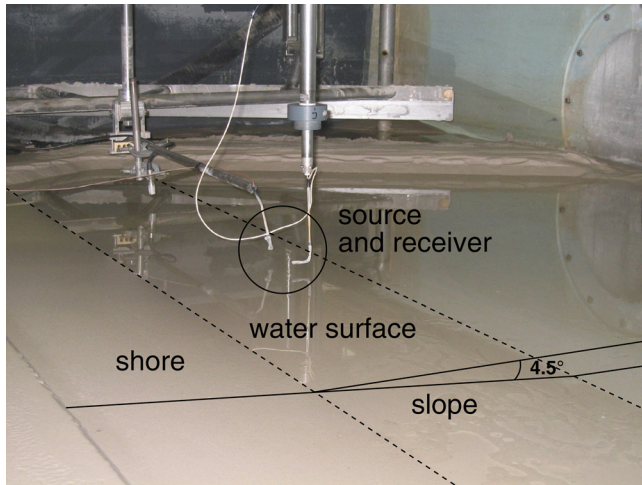


FIG. 1. (Color online) View of the shallow water tank (facilities of the LMA-CNRS laboratory) used in the experimental campaign, showing the source and the receiver both aligned along the across-slope direction of the wedge-shaped waveguide. The rake that was used to tilt the sandy bottom with a sloping angle of  $\approx 4.5^\circ$  can be seen on the background.

at the indoor shallow-water tank of the LMA-CNRS laboratory in Marseille. The inner tank dimensions are 10-m-long, 3-m-wide, and 1-m-deep. As illustrated in Fig. 1, a thin layer of water overlies a thick layer of calibrated river sand simulating a bottom half-space. A sloping bottom geometry with the wedge apex oriented lengthwise over the entire length of the tank was produced using a rake inclined at  $4.5^\circ$  (visible in the background of Fig. 1). The water depth at the source was measured using a separate high-frequency transducer (not shown here) yielding 48 mm, though one may expect an error of about 10%. Indeed, an overestimate of approximately 1 mm was attributed to surface tension effects in the very near vicinity of the transducer, whereas non-negligible evaporation relative to the water depth was observed during the measurements. The sound speed in the bottom was measured on sand samples to avoid damaging the bottom geometry, leading to 1660 m/s. However, during the calibration phase over a flat bottom,<sup>20</sup> it appeared more reasonable to consider a value within  $(1700 \pm 50)$  m/s due to an apparently different consolidation of the sand in the tank. The density of the sandy bottom was measured to be  $(1.99 \pm 0.01)$  g/cm<sup>3</sup>. The value of the bottom sound attenuation could not be measured at the central frequency (150 kHz) considered in the tank experiment (see discussion hereafter). The value of  $(0.5 \pm 0.1)$  dB per wavelength attributed to the attenuation at 150 kHz was extrapolated from attenuation values measured at higher frequencies. It is to be noticed that this value is a typical value for the specific type of sediment used. Most important is that this specific value permitted successful comparisons between theory and experiment during the calibration phase (see Ref. 20).

The source and receiver, illustrated in Fig. 1, were piezoelectric transducers having cylindrical shapes with 6-mm external diameter. Prior to the measurements, the signal used for transmission at the source was analyzed in a deep-water tank in order to avoid unwanted echoes. The signal recorded at 68 mm from the source is shown in the left panel of Fig. 2 where it appears well separated in time from its echoes (top

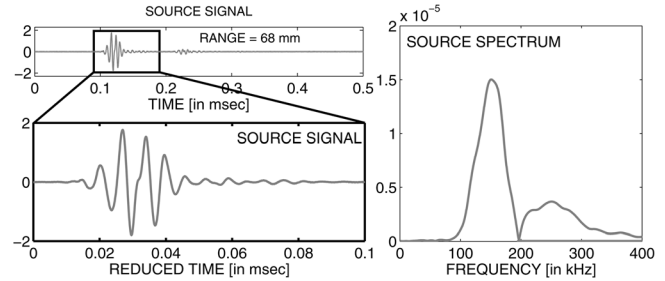


FIG. 2. Source signal (left) and its spectrum (right).

left panel). It is a five-cycle pulse with Gaussian envelope with 0.04 ms duration and with a weak tail of approximately the same duration due to the mechanical response of the transducer. Its frequency spectrum (right panel of Fig. 2) presents a main lobe centered at 150 kHz with a 100 kHz bandwidth as well as a secondary lobe above 200 kHz attributed to the distortion in the time signal observed at 0.03 ms (bottom left panel of Fig. 2). Note here that a 2-D normal mode code predicts that four trapped modes are excited at the source for the frequency of 150 kHz. During the measurements in the shallow-water tank, the source was kept at a fixed position and the receiver was moved within a vertical plane in the across-slope direction (parallel to the wedge apex). The received time signals were recorded in a time window of 5 ms at a rate of 10 MHz and averaged over five repeated measurements. An embankment of sand along the side-walls on the deep-water side of the tank achieved significant attenuation of the unwanted reflections in the recorded signals. Note, however, that the use of short pulses for transmission allows discarding the unwanted reflections by appropriate choice of a truncation window.

The focus in this paper is on two main data sets that were collected during two different days in a same week. The first data set provided fine sampling of the sound field in range and is herein referred to as ASP-H (for horizontal measurements of across-slope propagation). This data set consists of time signals recorded at a fixed receiver depth and at several source/receiver separations ranging from  $r = 0.1$  m to  $r = 5$  m in increments of 0.005 m. The measurements were repeated for three distinct source depths (SD), namely, 10 mm (all modes excited), 19 mm (mode 3 weakly excited), and 26.9 mm (modes 2 and 4 weakly excited), giving rise to three distinct data subsets herein referred to as ASP-H1, ASP-H2, and ASP-H3, respectively. The second data set provided fine sampling of the sound field in depth, at several coarser source/receiver separations and is herein referred to as ASP-V (for vertical measurements of across-slope propagation). The time signals in this data set were recorded at consecutive ranges from the source in 0.1 m increments where at each range they were recorded at several receiver depths from  $z_R = 1$  mm to  $z_R = 44$  mm in increments of 1 mm. The water sound speed was deduced from the temperature of the water,<sup>21</sup> which was  $21.95^\circ$  (respectively,  $22.13^\circ$ ) during the ASP-H1 measurements (respectively, ASP-H2 and ASP-H3), thus leading to a water sound speed of 1488.15 m/s (respectively, 1488.7 m/s), and  $22.19^\circ$  during the ASP-V measurements leading to 1488.9 m/s.

Figure 3 shows stacked time series versus range in the across-slope direction as recorded, from left to right, during the ASP-H1, ASP-H2, and ASP-H3 measurements respectively. The time series have been scaled appropriately to compensate for cylindrical spreading.

Overall, four modes can be identified by inspection of the depth stacks from the ASP-V data set (not shown here, see Ref. 22), denoted M1, M2, M3, and M4, respectively. The range stacks in Fig. 3 exhibit multiple mode arrivals, mode shadow zones, and intra-mode interference, which are typical 3-D effects identical to those described in the literature for the wedge-like environment.<sup>17,18</sup> For instance, at some range, mode 2 (denoted M2) presents two distinct arrivals that progressively overlap (i.e., interfere) as the receiver moves out in range across-slope, and eventually reaches its cut-off range beyond which its shadow zone extends. For a detailed description of the 3-D effects observed in the measurements, the reader is referred to Ref. 22. We note here the effect of the source depth being in the vicinity of a node of mode 3 in Fig. 3(b), and in the vicinity of the nodes of mode 2 and 4 in Fig. 3(c).

Let us conclude this section with two observations. First of all, in Fig. 3(a), we observe a slight unexpected delay in the arrival times of the recorded signals beyond the range of 3.5 m, which becomes significant beyond the range of 4.5 m. This delay, which is clearly not present in the ASP-H2 and ASP-H3 data sets, is likely due to a malfunction of the stepping mechanism moving the receiver during the ASP-H1 measurement. Finally, it is to be noticed that the noise-like signals observed, e.g., between the two arrivals of mode 1

beyond the range of 4 m in Fig. 3, pertain to the secondary lobe of the frequency spectrum in Fig. 2. These two issues will be further discussed in Sec. IV where the data are compared to numerical simulations.

### III. REFINEMENT OF MODEL PARAMETERS

A first, although encouraging, comparison of broadband predictions provided by a 3-D parabolic equation based code using the measured parameter values from the model experiment suggested a refinement was required. A simple inversion procedure is thus used to provide estimates of the parameters affecting propagation.

#### A. Inversion approach

The inversion is implemented in a Bayesian framework following the derivation by Refs. 23 and 24. In the Bayesian formulation, the solution to the inverse problem is fully characterized by the posterior probability density (PPD) of the parameters. Let the  $N$ -length complex vector  $\mathbf{d}_l$  denote the spectral components of the observed data recorded on a  $N$ -element receiving array at frequency  $f_l$ , and the  $M$ -length vector  $\mathbf{m}$  denote the parameters to be recovered. The PPD, defined as the probability density function (pdf) of  $\mathbf{m}$  given  $\mathbf{d}_l$ , is written as

$$p(\mathbf{m} | \mathbf{d}_l) = \frac{\mathcal{L}(\mathbf{m})p(\mathbf{m})}{\int_{\mathcal{M}} \mathcal{L}(\mathbf{m}')p(\mathbf{m}')d\mathbf{m}'}, \quad (1)$$

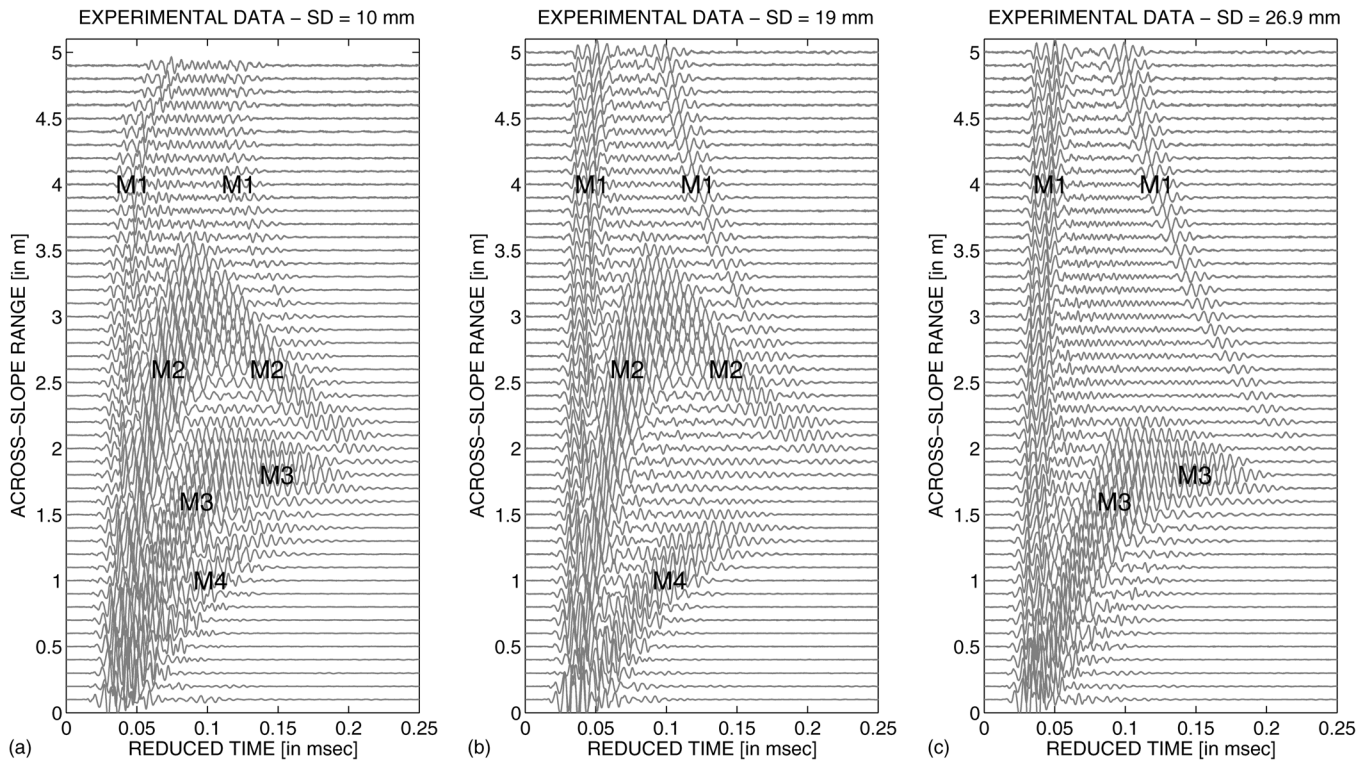


FIG. 3. Experimental signals extracted from the ASP-H data set. Stacked time series versus source/receiver range corresponding to the experimental data recorded along the across-slope direction for a source depth of (a) 10 mm (ASP-H1 data; all modes are excited), (b) 19 mm (ASP-H2 data; mode 3 is weakly excited), (c) 26.9 mm (ASP-H3 data; both modes 2 and 4 are weakly excited). For each panel, the receiver depth is 10 mm.

where  $\mathcal{L}(\mathbf{m})$  is the likelihood function,  $p(\mathbf{m})$  is the prior pdf reflecting *a priori* knowledge on the parameters, and the integration in the denominator is taken over the whole parameter space  $\mathcal{M}$ . The likelihood function gives a measure of fit between the observed data vector and the replica vector  $\mathbf{w}_r(\mathbf{m})$  provided by an ocean acoustic propagation model. It takes various forms depending on the amount of the data exploited in the inversion.<sup>25</sup> Likelihood functions used in this paper are derived under the assumption of additive complex Gaussian distributed errors. They are given in the Appendix and the reader is referred to Ref. 25 for a detailed discussion. For the purpose of this work, the PPD is sampled over the parameter space using exhaustive search, also known as a grid search.<sup>23,26</sup> This requires defining bounds for each parameter and discretizing the resulting search intervals. In practice, a replica vector is generated for each combination of the discrete values of the parameters and the major part of the central processing unit (CPU) time is spent on this task alone. A convenient estimate of  $\mathbf{m}$  for experiment-versus-theory comparisons is the maximum *a posteriori* (MAP) estimate obtained by maximizing the PPD. The posterior mean estimate and standard deviation, along with the posterior marginal densities, can be used to assess the quality and dispersion of the estimate.

## B. Parameterization

The assumptions on the environmental model adopted for replica generation are similar to those of the synthetic 3-D ASA wedge benchmark (see, e.g., Ref. 27), i.e., a water layer of constant sound speed lying over a fluid bottom half-space with constant parameters (sound speed, density, and sound attenuation), and a water/bottom interface presenting a constant slope. Point source and receivers are considered and the vertical plane containing them, referred to as the observation plane, is oriented in the across-slope direction (i.e., perpendicular to the slope) along which the water depth is constant and equal to the water depth at the source.

The parameters that are to be refined are those that can significantly affect the acoustic field within their margins of uncertainty. In the actual experimental context and for the considered operational frequencies, these are the water depth, the source and receiver depths, the slope, and the bottom parameters. Indeed, as discussed in Sec. II, the measured value of the water depth, denoted  $h_S$ , appeared to be overestimated and has thus to be included in the parameterization of the inverse problem. Because of the large dimension of the transmitting and receiving transducers relative to the water depth, the source and receiver depths, respectively, denoted  $z_S$  and  $z_R$ , are also included in the parameterization in order to obtain equivalent point source and receiver depths that provide the best match between experiment and theory. Furthermore, the sloping geometry of the sandy bottom was created using a rake inclined at  $4.5^\circ$  thus resulting in a slope of approximately the same value. It is also included in the parameterization in an effort to obtain a more accurate estimate.

Finally, although the assumption of a fluid bottom half-space with constant parameters might not exactly reflect reality at the considered frequencies, it yielded excellent comparisons

between experiment and theory during the calibration phase over a flat bottom.<sup>20</sup> In particular, the values of  $1.99 \text{ g/cm}^3$  and  $0.5 \text{ dB per wavelength}$  were used, respectively, for the bottom density and the sound attenuation in the bottom (see discussion in Sec. II), whereas a reasonable value for the bottom sound speed appeared to be  $1700 \text{ m/s}$ . We anticipate that inverting for an equivalent constant bottom sound speed yields estimates that are not well resolved, resulting in values that appear to be frequency and/or range dependent. The bottom parameters are thus kept fixed during the inversion at their respective values mentioned above. The parameterization of the inverse problem can thus be expressed as  $\mathbf{m} = [h_S, z_S, z_R, \text{slope}]^T$ . Other parameters involved in the environmental model are kept fixed at their nominal values during the inversion.

## C. Inversion setup

At first glance, the prominent 3-D effects observed in the recorded time signals suggest that the use of fully 3-D computations is necessary for replica generation. However, an inversion based on 3-D computations quickly becomes impractical for more than two parameters at a time due to the dramatically increased CPU times. This is true even with the use of more elaborate and efficient sampling algorithms than exhaustive search. In a recent work, it was shown that the slope effect onto inversions of simulated vertical array data in a 3-D wedge test case can be neglected at relatively short ranges from the source.<sup>28</sup> In other words, an inversion based on a 2-D model succeeds in retrieving the correct parameter values at short ranges. Applying this observation to the actual experimental context suggests that an inversion of vertical array data be performed in two steps as follows.

Step 1: inversion of short range vertical array data based on 2-D computations for the refinement of the so-called geometrical parameters, i.e., the water depth, the source depth, and the receiver depths, which are known to be dominant close to the source.

Step 2: inversion of vertical array data at farther ranges, where propagation is strongly affected by 3-D effects, for the recovery of the slope while keeping the geometrical parameters fixed at their MAP estimates deduced from the first step.

It is understood that the second inversion step requires 3-D computations for replica generation. Furthermore, it was shown that the objective function is highly sensitive to the slope whenever the array is positioned in the vicinity of the caustic or cut-off range of a single mode.<sup>28</sup> This observation is useful for choosing appropriate vertical array ranges in the second step. The two-step inversion approach can thus be applied on the ASP-V data set (described in Sec. II) where, for a given range, the consecutive fine measurements in depth can be viewed as measurements on a synthetic vertical array. When it comes to comparisons with ASP-H1, ASP-H2, and ASP-H3 data sets, new inversions are required in order to refine the geometrical parameters that are expected to be slightly different due to evaporation and subsequent refilling of the tank with fresh water. Here, for given source and receiver depths, the consecutive fine measurements in range are viewed as measurements on a synthetic horizontal array. Note now that the relative phase along a horizontal

array is sensitive to the 3-D variability of the acoustic field, even at short ranges. Therefore, the inversion of the ASP-H data set require replica generated by 3-D computations, which will now be using the MAP estimate of the slope from the two-step inversion. The choice of appropriate array position and aperture is thus constrained by the increased CPU times needed for a 3-D-model-based inversion.

## D. Inversion results

The observed data vector  $\mathbf{d}_l$  is composed of spectral components of the 4096-point windowed and Fourier-transformed time signals recorded at consecutive receiver positions forming a synthetic array. In each inversion five frequency bins are used: 131.8, 141.6, 151.3, 161.1, and 170.8 kHz. For each frequency, the replica vector  $\mathbf{w}_l(\mathbf{m})$  is generated at a scale of 1000:1 using the parabolic equation based code 3DWAPE (Ref. 29) for both 2-D and 3-D computations. The prior pdf  $p(\mathbf{m})$  is chosen uniform within the search intervals of each parameter (as given in the abscissa of Figs. 4 and 5) and zero elsewhere. The discretization is sufficiently fine to ensure convergence.

### 1. Two-step inversion of ASP-V data set

In both steps of ASP-V data inversion, a synthetic vertical line array composed of 40 receivers at nominal depths from 5 to 44 mm with a 1 mm depth increment is used. In the first inversion step the separation from the source is 0.1 m, whereas the ranges for the second step are chosen in the vicinity of mode-2 caustic occurring, for each respective frequency, at 2.6, 2.8, 2.9, 3.1, and 3.2 m from the source.

The PPD in Eq. (1) is evaluated using the likelihood function defined in Eq. (A3) which is equivalent to correlating observed and predicted complex acoustic field vectors. Recall that the first step is based on 2-D computations, whereas the second step requires 3-D computations. Accordingly, the single-processor CPU time for a single-frequency inversion is approximately 5 min in the first step (requiring 1891 replica vector generation), whereas it ranges from 3 to 5 h in the second step (requiring 25 replica vector generation). Figure 4 shows posterior marginal densities of the refined parameters in the first [Fig. 4(a)] and second [Fig. 4(b)]

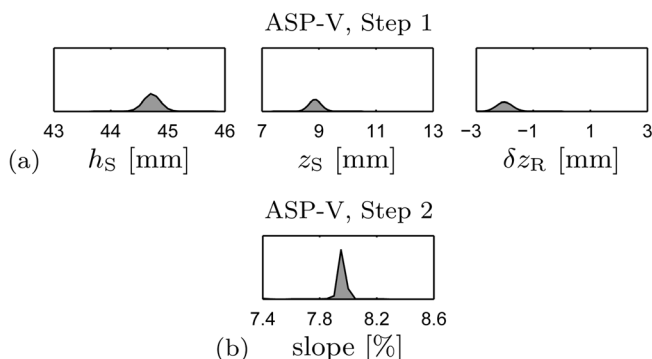


FIG. 4. Posterior marginal densities of (a) the water depth,  $h_S$ , the source depth,  $z_S$ , and the receiving array depth offset,  $\delta z_R$ , obtained in the first inversion step of ASP-V data set, (b) the slope obtained in the second inversion step of ASP-V data set.

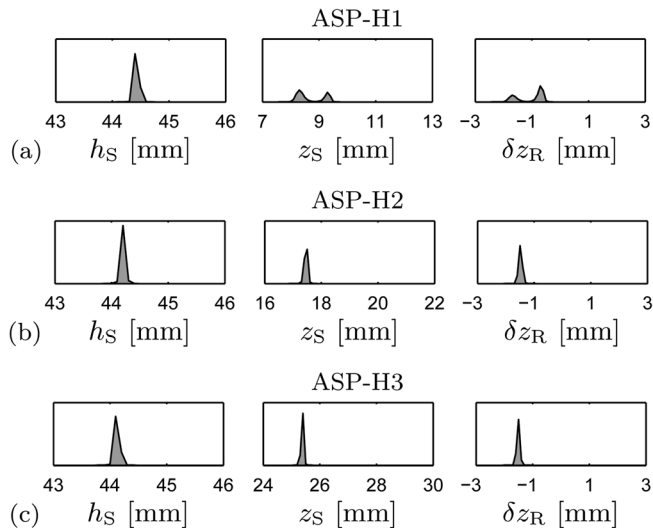


FIG. 5. Posterior marginal densities of the water depth,  $h_S$ , the source depth,  $z_S$ , and the receiving array depth offset,  $\delta z_R$ , obtained from inversions of (a) ASP-H1, (b) ASP-H2, and (c) ASP-H3 data sets.

inversion steps. The resulting estimates are summarized in Table I. Overall, the marginal densities present narrow concentrations around the mean estimates and are relatively symmetric so that the means coincide with the MAP estimates. Note the steep peak in Fig. 4(b) as a result of the importance of the slope in the vicinity of the mode-2 caustic.

### 2. Inversion of ASP-H data set

A synthetic horizontal line array is used here, composed of 16 receivers at nominal ranges from 0.15 to 0.3 m with a 0.01 m range increment and at a nominal depth of 10 mm. The PPD is now evaluated using the likelihood function defined in Eq. (A7) which is equivalent to fitting the transmission loss curves along the horizontal array. The inversion is repeated for each of the ASP-H1, ASP-H2, and ASP-H3 data sets, recalling that they were obtained for three distinct nominal source depths at 10, 19, and 26.9 mm, respectively. The inversion of horizontal data, requiring 3-D computations, resulted in 4 to 6 h CPU times for a single frequency. Figure 5 shows posterior marginal densities of the refined parameters for each of the three inversions, with resulting estimates given in Table I. Overall, similar observations apply here except for the notable multimodal character of the marginals of the source depth and the receiver depth offset in the ASP-H1 inversion. The two-dimensional posterior marginal density for these two parameters (not shown here) reveals a strong negative correlation, suggesting that, although the MAP estimate strictly results in  $(z_S, \delta z_R) = (8.30, -0.7)$  mm, the choice  $(z_S, \delta z_R) = (9.30, -1.7)$  mm is also acceptable. In other words, we expect that positioning the source 1-mm deeper and the receiving array 1-mm shallower yields a similar quality of fit between experimental and simulated transmission loss curves. We note that in this case the mean estimate has no meaning as it only gives the average of the two peaks. Note finally the decrease in the estimated value of the water depth from ASP-H1 to ASP-H3 inversion, most probably due to evaporation during the day the data were collected.

TABLE I. MAP estimates, posterior mean estimates ( $\mu$ ), and standard deviations ( $\sigma$ ) for parameters involved in the inversion of ASP-V and ASP-H data sets.

Parameter	ASP-V, Step 1			ASP-H1			ASP-H2			ASP-H3		
	MAP	$\mu$	$\sigma$	MAP	$\mu$	$\sigma$	MAP	$\mu$	$\sigma$	MAP	$\mu$	$\sigma$
$h_S$ [mm]	44.70	44.72	0.15	44.40	44.42	0.04	44.20	44.20	0.01	44.10	44.12	0.04
$z_S$ [mm]	8.90	8.87	0.22	8.30	8.69	0.47	17.50	17.46	0.06	25.40	25.39	0.02
$\delta z_R^a$ [mm]	-2.00	-2.01	0.27	-0.70	-1.06	0.47	-1.50	-1.48	0.06	-1.50	-1.51	0.05
	ASP-V, Step 2											
slope [%]	7.95	7.95	0.04									
slope angle [deg.]	4.55	4.55	0.02									

<sup>a</sup> $\delta z_R$  is defined as the depth offset of the receiving array with respect to its nominal depth.

#### IV. NUMERICAL SIMULATIONS AND COMPARISONS

In this section we compare numerical simulations obtained using the 3-D parabolic equation based model 3DWAPE (Ref. 29) to the ASP-H1, ASP-H2, and ASP-H3 experimental data sets. For convenience, in all the simulations, a scale factor of 1000:1 was used with respect to the experimental configuration. Note that, as in Ref. 15, the scale factor of 1000:1 was applied in all the simulations, where the frequencies and lengths have been appropriately modified (but keeping the 0.5 dB per wavelength value for the compressional attenuation coefficient in the fluid bottom layer), to show the analogy between propagation in the tank and an oceanic waveguide. The wedge-shaped computational domain consists of a lossless homogeneous water layer with the relevant value of the sound speed (1488.2 m/s for ASP-H1, and 1488.7 m/s for both ASP-H2 and ASP-H3) and a density of 1 g/cm<sup>3</sup>, overlying a lossy half-space sediment bottom truncated at a depth of 600 m below the seafloor, with a homogeneous sound speed of 1700 m/s, a density of 1.99 g/cm<sup>3</sup>, and a sound attenuation of 0.5 dB per wavelength. For each comparison, separate runs of the 3-D PE code were performed using the MAP estimates of the geometrical parameters as given in Table I for the respective data set. In all the comparisons, the slope of the tilted bottom was set equal to 4.55° corresponding to the MAP estimate from the second inversion step of the ASP-V data (first column of Table I). The maximum computation range was set to 5 km.

##### A. Comparisons in the time domain

In 3DWAPE, the broadband computations are carried out using a Fourier-synthesis approach. Since the time arrivals in the problem at hand are essentially dominated by contributions pertaining to the main lobe of the spectrum of the source signal (see Fig. 2), only frequencies below 196 kHz were considered in the computations. In practice, this involves the following steps. First, the source signal recorded in the deep-water tank (Fig. 2) is decomposed using a Fourier transform. Then, consecutive runs of the 3-D PE code are performed for each uniformly distributed frequency over the range from 50 to 196 Hz (recall that a scale factor of 1000:1 is used) at frequency intervals of  $\Delta f = 0.25$  Hz (this leads to 585 discrete frequencies). Note that in this manner, the acoustic field is being set to zero for any frequency outside this frequency

band, and the frequency content of the source signal above 196 kHz is thus being neglected. The last step involves reconstructing the time signals at each receiver range and depth by means of an inverse Fourier transform.

The simulated stacked time series versus range in the across-slope direction plotted in Fig. 6 were obtained running the 3-D PE code where, from left to right, the source depth is 8.3, 17.5, and 25.4 m, respectively, corresponding to the MAP estimate obtained from the inversion of the respective ASP-H1, ASP-H2, and ASP-H3 data sets (see Table I). We note here that the nominal receiver depth has been corrected according to the depth- offset estimates given in Table I, i.e., the receiver depth in the computations was set to  $10 - 0.7 = 9.3$  m in Fig. 6(a) and  $10 - 1.5 = 8.5$  m in Figs. 6(b) and 6(c). As previously done in Fig. 3, the simulated time series in Fig. 6 have been scaled to compensate for cylindrical spreading. Overall, we observe a very good agreement with the experimental results of Fig. 3. Note that the simulated time series in Fig. 6(a) do not exhibit the time delay observed in Fig. 3(a) beyond the range of 3.5 m, thus confirming that the delay was due to a malfunction of the positioning mechanism of the receiver (see discussion in Sec. II).

Before proceeding to detailed comparisons, let us discuss the simulated results of Fig. 7 illustrating the depth-versus-time representations of the envelope of the simulated signals at successive ranges (from 0.5 to 4.5 km) and providing a more complete picture of the evolution of the modal structure of the propagating signals with range. This representation gives clear evidence of the 3-D effects occurring over a tilted bottom for each propagating mode. Indeed, the multiple arrivals of each mode are clearly observed at some ranges, e.g., two distinct arrivals of mode 2 are identified at the range of 2.5 km, overlapping (thus interfering) at 3 km, vanishing progressively with increasing range (see at 3.5 km), and leaving a shadow zone for mode 2 at the ranges of 4 and 4.5 km.

Detailed comparisons between numerical and experimental results are shown in Fig. 8, where the simulated time series from Fig. 6(a) (for a source depth of 8.3 m) are superimposed on the ASP-H1 experimental time series from Fig. 3(a) for some selected ranges from the source. For comparison purpose, the experimental scale is used, so that the time is expressed in milliseconds and the source/receiver range in

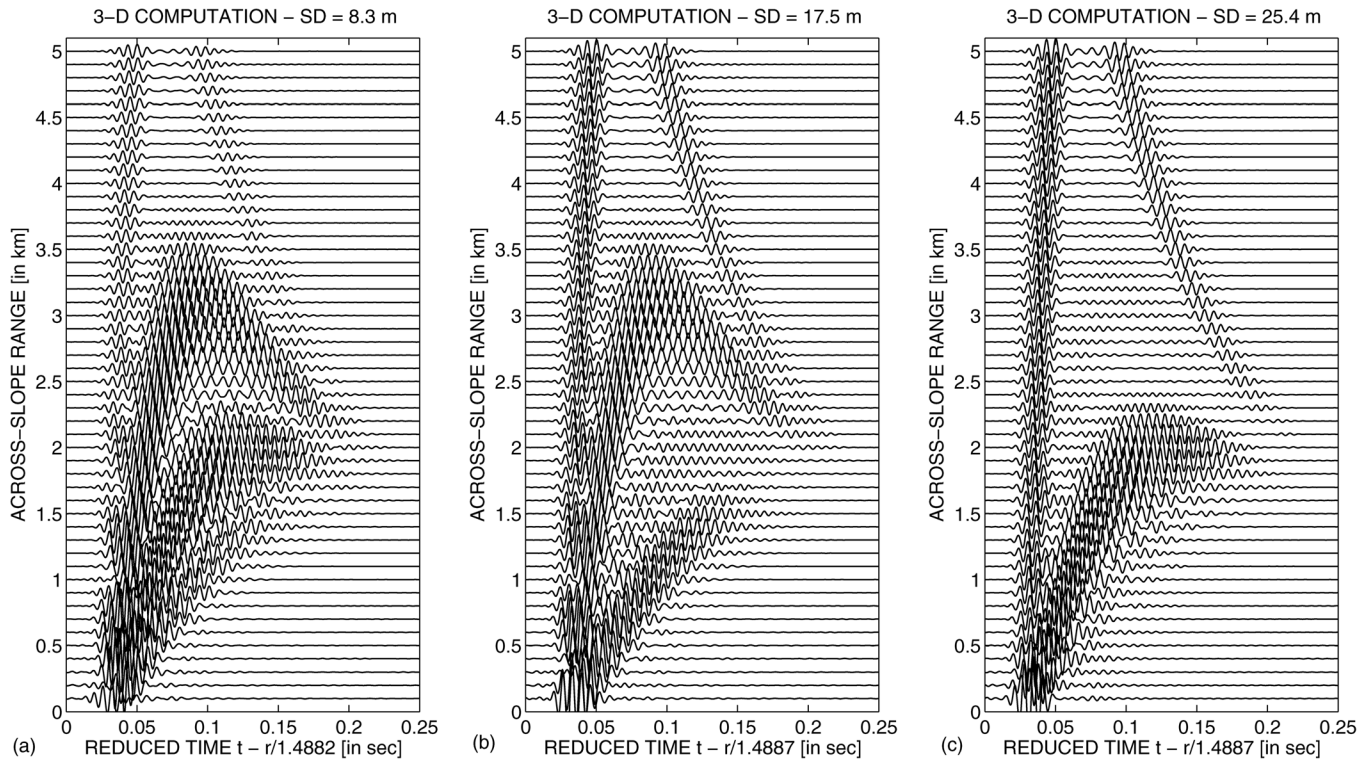


FIG. 6. Results of 3-D numerical simulations with 3DWAPE with a scale factor of 1000:1. Stacked time series versus source/receiver range in the across-slope direction for a source depth of (a) 8.3 m (all modes are excited), (b) 17.5 m (mode 3 is weakly excited), (c) 25.4 m (both modes 2 and 4 are weakly excited) and at a receiver depth of (a) 9.3 m, (b) and (c) 8.5 m.

meters. In addition, the amplitude of both numerical and experimental signals has been normalized to unity by dividing, at each range, the time series by their maximum values. Note finally that the experimental signals have been

low-pass filtered (with a cut-off frequency of 196 kHz) in order to remove the higher-frequency content that was not taken into account in the 3-D PE broadband computations. For each receiver range, we observe a very good agreement,

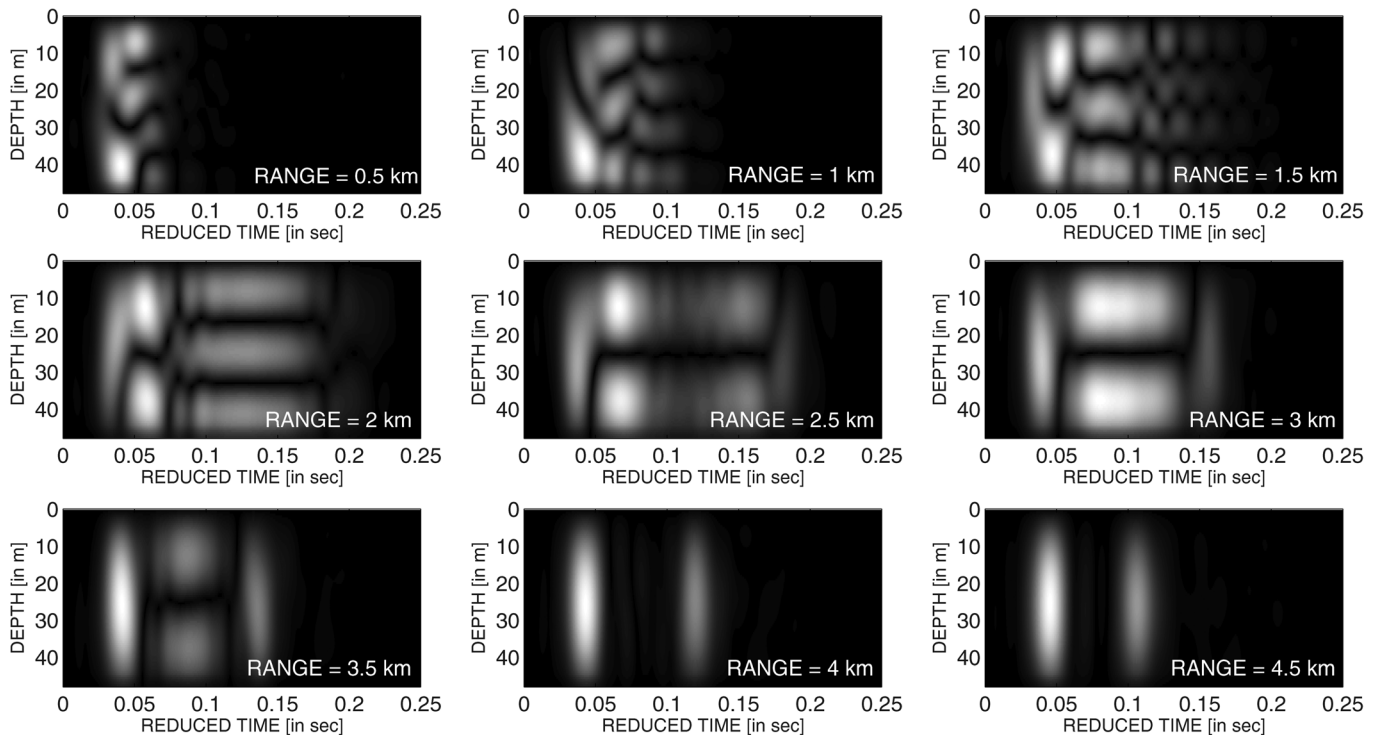


FIG. 7. Results of 3-D numerical simulations with 3DWAPE with a scale factor of 1000:1. Depth-versus-time representation at successive source/receiver ranges (from 0.5 to 4.5 km) in the across-slope direction. The source depth is 8.3 m (all modes are excited) and the water depth is 44.4 m.

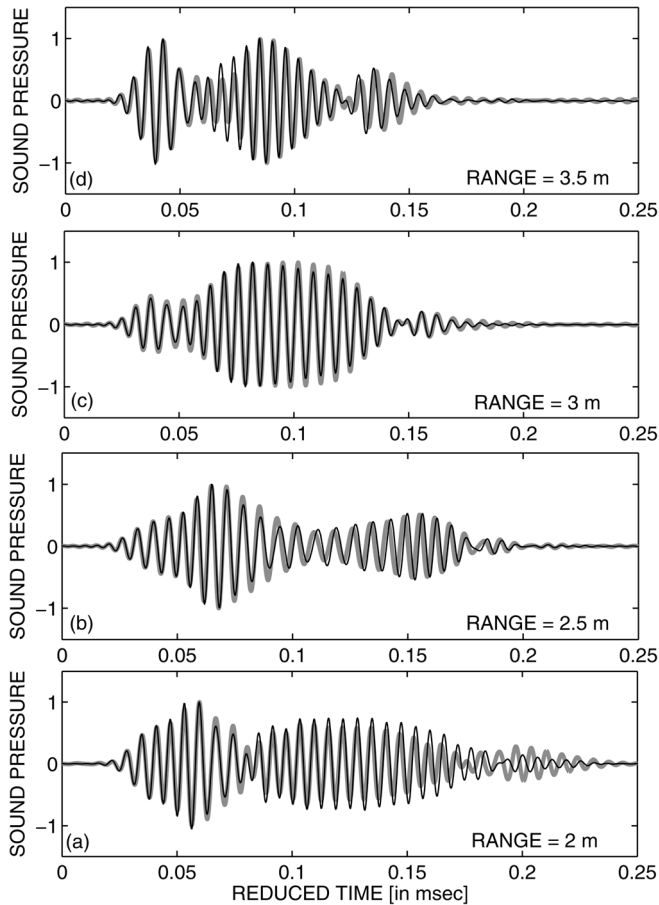


FIG. 8. Comparisons in the time domain. Time series in the across-slope direction at a fixed receiver depth and several ranges: (a) 2 m, (b) 2.5 m, (c) 3 m, and (d) 3.5 m. For each subplot, the thick gray line corresponds to the experimentally recorded ASP-H1 data (source depth: 10 mm; receiver depth: 10 mm) and the thin black line corresponds to the numerical solution (source depth: 8.3 m; receiver depth: 9.3 m) obtained running the 3-D PE based code 3DWAPE.

both in phase and relative amplitude, between the experimental and simulated results, demonstrating that the 3-D PE broadband computations are able to reproduce the experimentally recorded data with fine details.

## B. Comparisons in the frequency domain

Predicted transmission loss (TL) versus across-slope range obtained with the 3-D PE code are now compared to experimental TL curves. The experimental TL curves are extracted from the ASP-H data set, at any desired frequency within the bandwidth of the source signal, by means of Fourier transforms of the time series. Recall that during the ASP-H1, ASP-H2, and ASP-H3 measurements, as described in Sec. II, the time signals were recorded at a single receiver depth (10 mm) and at several distances between 0.1 and 5 m with a range increment of 0.005 m, thus providing a sufficiently fine representation of the acoustic field in range.

Let us first compare the numerical results to the experimental data at the frequency of 150 kHz, being close to the dominant frequency of the source signal. The comparisons are displayed in Fig. 9. The experimental TL curves are represented by the gray traces connecting the experimental data points indicated by the data markers. From top to bottom,

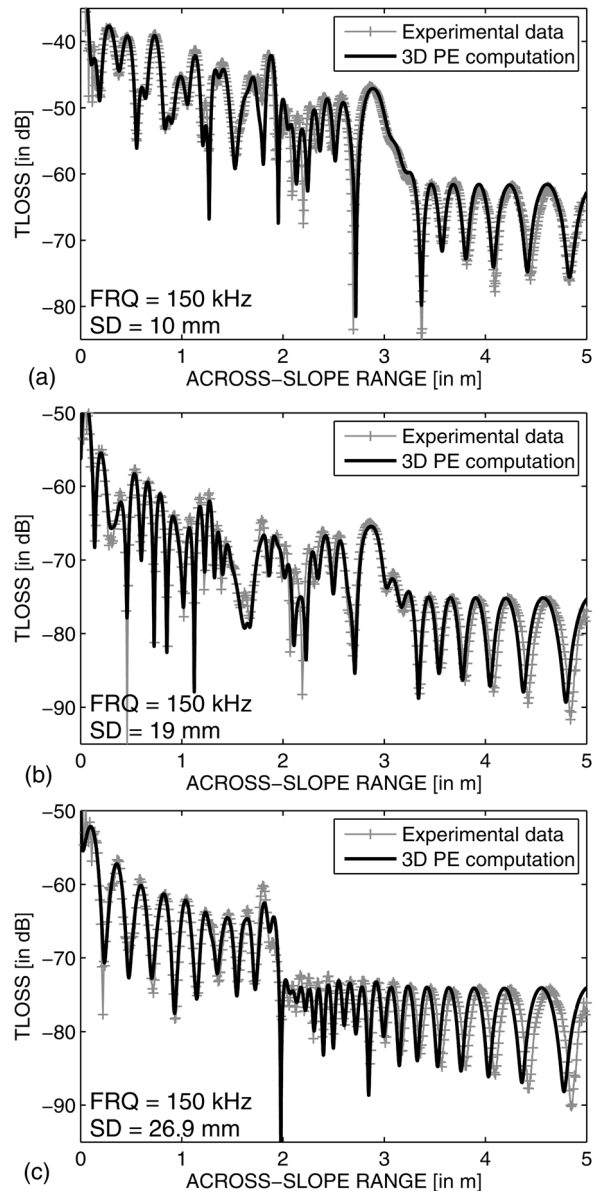


FIG. 9. Comparisons in the frequency domain. TL-versus-range curves (receiver depth: 10 mm, across-slope direction) at 150 kHz extracted from the experimental data (gray lines with data marker) corresponding to a source depth of (a) 10 mm (ASP-H1; all modes are excited), (b) 19 mm (ASP-H2; mode 3 is weakly excited), (c) 26.9 mm (ASP-H3; both modes 2 and 4 are weakly excited). The black solid lines represent the corresponding 3-D PE solutions whose source and receiver depths are given in Table I.

the experimental TL curves were respectively extracted from the ASP-H1, ASP-H2, and ASP-H3 data sets, recalling that these correspond to nominal source depths of 10 mm (where all modes are excited), 19 mm (where mode 3 is weakly excited), and 26.9 mm (where both modes 2 and 4 are weakly excited), in the respective order. The black curves in Fig. 9 represent TL curves as predicted by the 3-D PE model 3DWAPE at a scale of 1000:1. Note, however, that the experimental scale is used (for time and range) on the figures for the purpose of comparison. Let us first note that the interference patterns in each curve of Fig. 9 reveal the cut-off ranges of each mode at the frequency of 150 Hz. Indeed, the ranges of 1.3, 2, and 3 m can be identified as the approximate cut-off ranges of modes 4, 3, and 2, respectively, where the

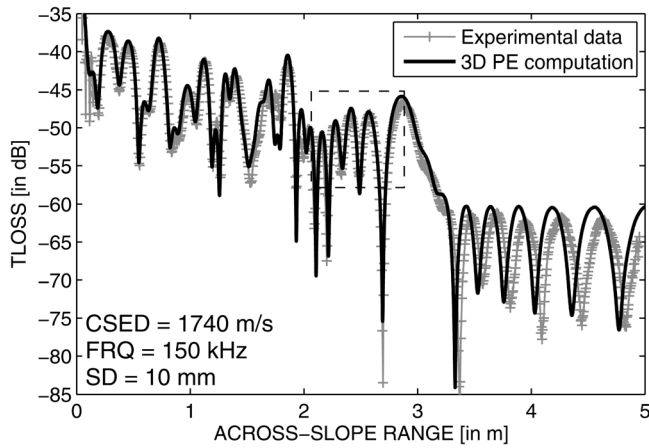


FIG. 10. Comparison in the frequency domain. TL-versus-range curve (receiver depth: 10 mm, across-slope direction) extracted from the ASP-H1 experimental data (gray line with data marker) at 150 kHz. The black solid line represents the corresponding 3-D PE solution whose source and receiver depths are given in Table I. The sound speed in the sediment is 1740 m/s (instead of 1700 m/s as in all other computations).

intensity abruptly decreases. The predicted TL curves in Fig. 9 are in very good agreement with the experimental ones. Nevertheless, a slight shift in phase can be observed at some ranges, as, for instance, between the ranges of 2 and

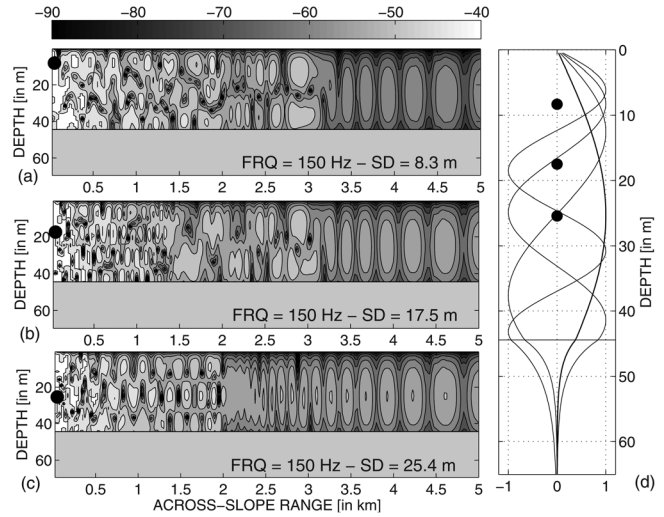
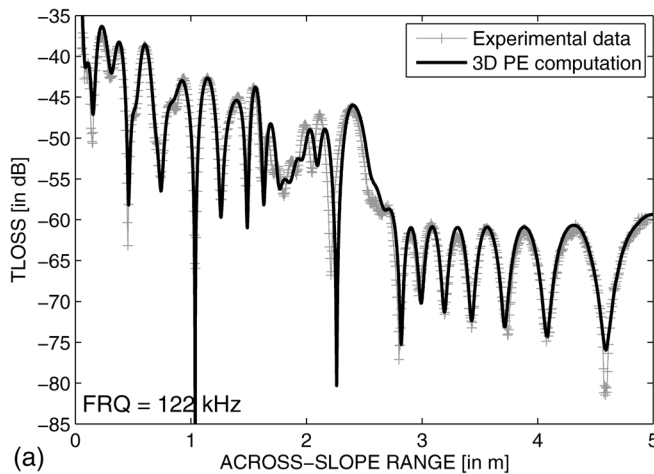
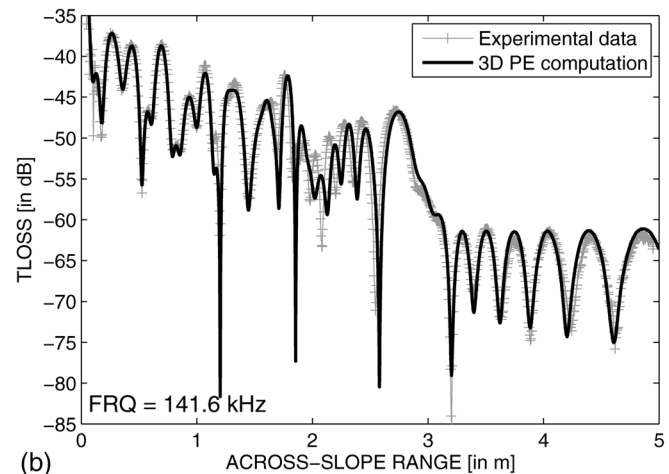


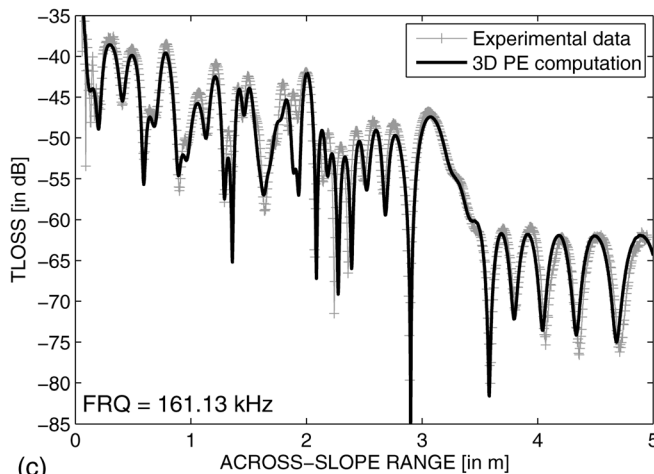
FIG. 11. Left panel: Transmission loss (in dB re 1 m) at 150 Hz (vertical slices in the across-slope direction) corresponding to 3-D PE computations with a scale factor of 1000:1 considering an omnidirectional point source located at a depth of (a) 8.3 m (all modes are excited), (b) 17.5 m (mode 3 is weakly excited), and (c) 25.4 m (both modes 2 and 4 are weakly excited). On the right panel are shown the shapes of the four propagating modes as a function of depth. On each panel, the position of the source is indicated by a black circle.



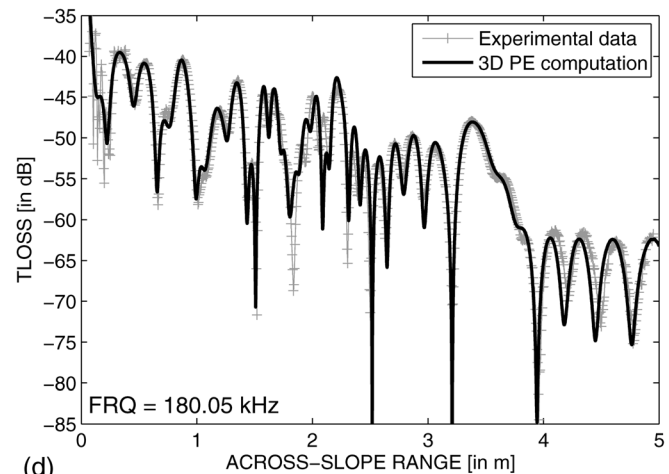
(a)



(b)



(c)



(d)

FIG. 12. Comparisons in the frequency domain at several frequencies. TL-versus-range curves (receiver depth: 10 mm, across-slope direction) extracted from the ASP-H1 experimental data (gray lines with data marker) at four frequencies: (a) 122 kHz, (b) 141.6 kHz, (c) 161.13 kHz, (d) 180.05 kHz. The source depth is 10 mm (all modes are excited). The black solid lines represent the corresponding 3-D PE solutions whose source and receiver depths are given in Table I.

3 m in Fig. 9(a), where the 3-D effects of mode 2 are more pronounced. It is worth noting that running the 3-D PE code with a different value for the sound speed in the sediment can lead to an improvement at some ranges but deteriorates the quality of the comparisons at others. For instance, the comparisons obtained carrying out the simulations with a homogeneous bottom sound speed of 1740 m/s (instead of 1700 m/s) are shown in Fig. 10. Note that this specific value of the bottom sound speed resulted in good comparisons over a flat bottom in the past. As seen in Fig. 10, the comparisons with the experimental data for a titled bottom, though better at some ranges (for instance, between 2 and 3 m) deteriorate significantly at longer ranges.

Overall, the 3-D PE model is able to accurately reproduce the acoustic field in the tank and correctly predict the 3-D propagation effects to which the modes are being subjected. Furthermore, by construction, the 3D PE computations provide the complete picture in the waveguide (i.e., in range, depth, and azimuth) without additional effort. For instance, Fig. 11 represents TL versus across-slope range and depth as computed by the 3DWAPE code for the respective comparisons of Fig. 9. In this representation, the cut-off ranges are recognized in a more straightforward manner.

Figure 12 shows comparisons of predicted and experimental TL curves extracted from the ASP-H1 data set at four additional frequencies: 122, 141.6, 161.13, and 180.05 kHz. At each frequency, the predicted TL curves closely track the detailed variations in the experimental TL curves, and this could be expected, since a broadband likelihood function was used when inverting the data. Note finally how the cut-off of each mode is shifted out in range with increasing frequency. This effect is known in the literature as the frequency dependence of the mode cut-off range.

## V. CONCLUDING REMARKS

In this paper, laboratory scale measurements of 3-D acoustic propagation in a penetrable wedge were compared with predictions by the 3-D parabolic equation code 3DWAPE. A first comparison using the parameter values measured in the tank, although encouraging, suggested a refinement was required. A subspace inversion approach, to overcome the significant CPU time requirements of 3-D computations, was used to refine the geometrical parameters (source depth, receiver depth, and water depth) and the slope, within the margins of their experimental uncertainties. The inversion of the data turned out to be a crucial step in successfully achieving the comparisons. Using the refined parameter values, the 3-D PE model was able to accurately reproduce the fine details of the measured 3-D acoustic field in the tank, both in the time and in the frequency domain, demonstrating the full potential of the model at hand. In addition, it is worth noting that, by construction, the 3-D PE model provides the entire acoustic field in the waveguide (in range, depth, and azimuth) with no additional effort.

Let us note that the strong assumption of a homogeneous bottom half-space adopted in the 3-D PE computations, though subject to discussion, turned out to be reasonable in the actual context. Among others, this assumption involves

neglecting the potential presence of shear waves propagating in the bottom when inverting the data. Note that the same assumption led to satisfactory agreement between theory and experiment during the calibration phase over a flat bottom, even though satisfactory comparisons were also achieved using a very low shear wave speed value. In its present form, the 3-D PE model 3DWAPE handles multilayered fluid bottoms alone, but can be modified to incorporate the effect of a low shear wave speed in the bottom using an equivalent fluid approximation based on the complex density approach proposed by Zhang and Tindle.<sup>30</sup> This modification, being quite straightforward and having already been successfully applied in a 3-D PE code,<sup>31</sup> will permit one to perform additional comparisons considering a shear-supporting bottom. This is currently underway. As a final note, the data collected during this experimental campaign have an overall promising potential to provide a real-data benchmark for 3-D model validation and performance comparison.

## APPENDIX: OBJECTIVE FUNCTIONS

Let the  $N$ -length complex vector  $\mathbf{d}_l$  denote the observed data at frequency  $f_l$  on an  $N$ -element receiving array at some location in the water column, and  $\mathbf{w}_l(\mathbf{m})$  the replica vector provided by an ocean acoustic propagation model as a function of the  $M$ -length parameters vector  $\mathbf{m}$  to be recovered. Assuming additive errors, the observed data and replica vectors are related through

$$\mathbf{d}_l = S_l \mathbf{w}_l(\mathbf{m}) + \mathbf{n}_l, \quad (\text{A1})$$

where  $S_l$  denotes the complex source strength at frequency  $f_l$  and  $\mathbf{n}_l$  the error vector including both experimental and theory errors. When the error term is assumed zero-mean complex Gaussian distributed with diagonal covariance matrix  $\nu_l \mathbf{I}$ , i.e., spatially uncorrelated, the broadband likelihood function is written

$$\mathcal{L}(\mathbf{m}; S, \nu) = \prod_{l=1}^L (\pi \nu_l)^{-N} \exp \left[ -\frac{\|\mathbf{d}_l - S_l \mathbf{w}_l(\mathbf{m})\|^2}{\nu_l} \right], \quad (\text{A2})$$

where it is further assumed that the errors are uncorrelated across frequency. When the source spectrum and the variance are unknown, they are replaced by their estimates obtained by maximizing Eq. (A2).

The first expression used herein is derived for complex acoustic pressure fields, i.e., using both magnitude and phase, following

$$\mathcal{L}_1(\mathbf{m}) = \prod_{l=1}^L (\pi \hat{\nu}_l)^{-N} \exp \left[ -\frac{\phi_{l,1}(\mathbf{m})}{\hat{\nu}_l} \right], \quad (\text{A3})$$

where  $\phi_{l,1}$  is an objective function related to the Bartlett power given as<sup>23–25</sup>

$$\phi_{l,1}(\mathbf{m}) = \|\mathbf{d}_l\|^2 - \frac{|\mathbf{w}_l^*(\mathbf{m}) \mathbf{d}_l|^2}{\|\mathbf{w}_l(\mathbf{m})\|^2}, \quad (\text{A4})$$

and  $\hat{v}_l$  is a global maximum likelihood estimate of the variance obtained as

$$\hat{v}_l = \frac{1}{N} \phi_{l,1}(\hat{\mathbf{m}}) \quad (\text{A5})$$

and evaluated at the maximum likelihood solution  $\hat{\mathbf{m}}$ . This latter is obtained by minimizing<sup>25</sup>

$$\Phi(\mathbf{m}) = \prod_{l=1}^L \phi_{l,1}(\mathbf{m}). \quad (\text{A6})$$

over all  $\mathbf{m}$ . Note here that  $N$  in Eq. (A5) should be replaced by the effective number of uncorrelated receivers along the array which is usually equivalent to the number of trapped modes contributing at the array.<sup>32</sup> The expression (A3) leads to the matched-field inversion technique where Eq. (A4) is recognized as the normalized Bartlett power.

The second expression of the broadband likelihood function used herein is derived using the magnitude of the data alone:

$$\mathcal{L}_2(\mathbf{m}) = \prod_{l=1}^L \phi_{l,2}(\mathbf{m})^{-N/2} \prod_{n=1}^N |w_{l,n}(\mathbf{m})|^{-1/2}, \quad (\text{A7})$$

where  $w_{l,n}(\mathbf{m})$  is the  $n$ th component of vector  $w_l(\mathbf{m})$  and the objective function is given as

$$\phi_{l,2}(\mathbf{m}) = \|\mathbf{d}_l\|^2 - \left( \frac{|\mathbf{w}_l(\mathbf{m})| * |\mathbf{d}_l|}{\|\mathbf{w}_l(\mathbf{m})\|} \right)^2. \quad (\text{A8})$$

Using Eq. (A7) is equivalent to fitting experimental and predicted transmission loss curves along the array.

<sup>1</sup>A. Tolstoy, "3-D propagation issues and models," J. Comput. Acoust. **4**, 243–271 (1996).

<sup>2</sup>K. D. Heaney and J. J. Murray, "Measurements of three-dimensional propagation in a continental shelf environment," J. Acoust. Soc. Am. **125**, 1394–1402 (2009).

<sup>3</sup>M. S. Ballard, Y.-T. Lin, and J. F. Lynch, "Horizontal refraction of propagating sound due to seafloor scours over a range-dependent layered bottom on the New Jersey shelf," J. Acoust. Soc. Am. **131**, 2587–2598 (2012).

<sup>4</sup>L. Y. S. Chiu, A. Y. Y. Chang, C.-F. Chen, R.-C. Wei, Y.-J. Yang, and D. B. Reeder, "Three dimensional acoustic simulation of an acoustic refraction by a nonlinear internal wave in a wedge bathymetry," J. Comput. Acoust. **18**, 279–296 (2010).

<sup>5</sup>D. B. Reeder, L. Y. S. Chiu, and C.-F. Chen, "Experimental evidence of horizontal refraction by nonlinear internal waves of elevation in shallow water in the South China Sea: 3D versus Nx2D acoustic propagation modeling," J. Comput. Acoust. **18**, 267–278 (2010).

<sup>6</sup>M. S. Ballard, "Modeling three-dimensional propagation in a continental shelf environment," J. Acoust. Soc. Am. **131**, 1969–1977 (2012).

<sup>7</sup>L. Hsieh, Y. Lin, and C. Chen, "Three dimensional wide angle azimuthal PE solution to modified benchmark problems," J. Acoust. Soc. Am. **115**, 2579 (2004).

<sup>8</sup>L. Hsieh, C. Chen, M. Yuan, and Y. Lin, "Azimuthal limitation in 3D PE approximation for underwater acoustic propagation," J. Comput. Acoust. **15**, 221–233 (2007).

<sup>9</sup>L. Y. S. Chiu, Y.-T. Lin, C.-F. Chen, T. F. Duda, and B. Calder, "Focused sound from three-dimensional sound propagation effects over a submarine canyon," J. Acoust. Soc. Am. **129**, EL260–EL266 (2011).

<sup>10</sup>M. E. Austin and N. R. Chapman, "The use of tessellation in three-dimensional parabolic equation modeling," J. Comput. Acoust. **19**, 221–239 (2011).

<sup>11</sup>P. Borejko, "An analysis of cross-slope pulse propagation in a shallow water wedge," in *Proceedings of the 10th Conference on Underwater Acoustics*, edited by T. Akal, Istanbul, Turkey (2010).

<sup>12</sup>Y.-T. Lin and T. F. Duda, "A higher-order split-step fourier parabolic-equation sound propagation solution scheme," J. Acoust. Soc. Am. **132**, EL61–EL67 (2012).

<sup>13</sup>Y.-T. Lin and J. F. Lynch, "Analytical study of the horizontal ducting of sound by an oceanic front over a slope," J. Acoust. Soc. Am. **131**, EL1–EL7 (2011).

<sup>14</sup>F. Sturm, "Investigation of 3-D benchmark problems in underwater acoustics: A uniform approach," in *Proceedings of the 9th European Conference on Underwater Acoustics*, edited by M. E. Zakharia, D. Cassereau, and F. Luppé, Paris, France (2008), Vol. 2, pp. 759–764.

<sup>15</sup>J. M. Collis, W. L. Siegmann, M. D. Collins, H. J. Simpson, and R. J. Soukup, "Comparison of simulations and data from a seismo-acoustic tank experiment," J. Acoust. Soc. Am. **122**, 1987–1993 (2007).

<sup>16</sup>J. D. Schneiderwind, J. M. Collis, and H. J. Simpson, "Elastic Pekeris waveguide normal mode solution comparisons against laboratory data," J. Acoust. Soc. Am. **132**, EL182–EL188 (2012).

<sup>17</sup>C. H. Harrison, "Acoustic shadow zones in the horizontal plane," J. Acoust. Soc. Am. **65**, 56–61 (1979).

<sup>18</sup>M. J. Buckingham, "Theory of three-dimensional acoustic propagation in a wedgelike ocean with a penetrable bottom," J. Acoust. Soc. Am. **82**, 198–210 (1987).

<sup>19</sup>F. Sturm, J.-P. Sessarego, and D. Ferrand, "Laboratory scale measurements of across-slope sound propagation over a wedge-shaped bottom," in *2nd International Conference & Exhibition on Underwater Acoustic Measurements: Technologies & Results*, edited by J. S. Papadakis and L. Björno, Heraklion, Crete, Greece (2007), Vol. 3, pp. 1151–1156.

<sup>20</sup>P. Papadakis, M. Taroudakis, F. Sturm, P. Sanchez, and J.-P. Sessarego, "Scaled laboratory experiments of shallow water acoustic propagation: Calibration phase," Acta Acust. Acust. **94**, 676–684 (2008).

<sup>21</sup>N. Bilaniuk and G. S. K. Wong, "Speed of sound in pure water as a function of temperature," J. Acoust. Soc. Am. **93**, 1609–1612 (1993).

<sup>22</sup>A. Korakas, F. Sturm, J.-P. Sessarego, and D. Ferrand, "Scaled model experiment of long-range across-slope pulse propagation in a penetrable wedge," J. Acoust. Soc. Am. **126**, EL22–EL27 (2009).

<sup>23</sup>P. Gerstoft and C. F. Mecklenbrauker, "Ocean acoustic inversion with estimation of a posteriori probability distributions," J. Acoust. Soc. Am. **104**, 808–819 (1998).

<sup>24</sup>S. E. Dosso and G. Birdsall, "Quantifying uncertainties in geoacoustic inversion I: A fast Gibbs sampler approach," J. Acoust. Soc. Am. **111**, 129–142 (2002).

<sup>25</sup>C. F. Mecklenbrauker and P. Gerstoft, "Objective functions for ocean acoustic inversion derived by likelihood methods," J. Comput. Acoust. **8**, 259–270 (2000).

<sup>26</sup>M. K. Sen and P. L. Stoffa, "Bayesian inference, Gibbs' sampler and uncertainty estimation in geophysical inversion," Geophys. Prospect. **44**, 313–350 (1996).

<sup>27</sup>J. A. Fawcett, "Modeling three-dimensional propagation in an oceanic wedge using parabolic equation methods," J. Acoust. Soc. Am. **93**, 2627–2632 (1993).

<sup>28</sup>A. Korakas and F. Sturm, "On the feasibility of a matched-field inversion in a three-dimensional environment ignoring out-of-plane propagation," IEEE J. Oceanic Eng. **36**, 716–727 (2011).

<sup>29</sup>F. Sturm, "Numerical study of broadband sound pulse propagation in three-dimensional oceanic waveguides," J. Acoust. Soc. Am. **117**, 1058–1079 (2005).

<sup>30</sup>Z. Y. Zhang and C. T. Tindle, "Improved equivalent fluid approximations for a low shear speed ocean bottom," J. Acoust. Soc. Am. **98**, 3391–3396 (1995).

<sup>31</sup>G. H. Brooke, D. J. Thomson, and G. R. Ebbeson, "PECAN: A Canadian parabolic equation model for underwater sound propagation," J. Comput. Acoust. **9**, 69–100 (2001).

<sup>32</sup>S. E. Dosso and G. Birdsall, "Quantifying uncertainties in geoacoustic inversion II. Application to broadband, shallow-water data," J. Acoust. Soc. Am. **111**, 143–159 (2002).